

Precise Interception Flight Targets by Image-based Visual Servoing of Multicopter

Hailong Yan, Kun Yang, Yixiao Cheng, Zihao Wang, and Dawei Li

Abstract—Interception of low-altitude intruding targets with low-cost drones equipped strapdown camera presents a competitive option. However, the malicious maneuvers by the non-cooperative target and the coupling of the camera make the task challenging. To solve this problem, an Image-Based Visual Servoing (IBVS) control algorithm based on proportional navigation guidance with field-of-view holding capability is designed. The proposed controller reduces the miss distance while improving the stability of the visual servo system during interception. Software-in-the-loop (SITL) simulation experiments show a 72.8% reduction in the circular error probability (CEP) compared to the most recent study. This improvement enhances interception accuracy from the decimeter to the centimeter level. Real-world experiments further validate the effectiveness of the proposed algorithm.

Index Terms—precise interception, IBVS, proportional navigation guidance, multicopter control

I. INTRODUCTION

THE presence of non-cooperative targets at low altitudes poses a significant threat to flight safety and hinders the development of low-altitude economies [1]–[4]. Commonly used countermeasures such as radio-frequency (RF) signal jamming [5], [6] and high-energy weapon shoot-downs [7], [8] are effective but have detrimental environmental impacts. The capture methods [9], [10] are environmentally friendly but less effective against moving targets. All these methods exhibit notable deficiencies when dealing with moving targets. The use of sensor-equipped unmanned aerial vehicles (UAVs) to intercept intruding targets has gained significant attention due to their rapid deployment, safety, and cost-effectiveness. Camera-based solutions, in particular, have shown great potential due to their low cost, lightweight, and high versatility [11]–[13].

Manuscript received September 24, 2024; revised Month xx, xxxx; accepted Month x, xxxx. (Corresponding author: Dawei Li.) **This paper is being reviewed.**

Hailong Yan is with the School of Computer Science, Northwestern Polytechnical University, Xi'an 710129, China. (e-mail: hlyan@mail.nwpu.edu.cn).

Kun Yang, Yixiao Cheng, and Dawei Li are with the School of Automation Science and Electrical Engineering, the School of Future Aerospace Technology, and the Institute of Unmanned Systems, respectively, Beihang University, Beijing 100191, China. (e-mail: yangkun_buaa@buaa.edu.cn; yixiao_cheng@buaa.edu.cn; david@buaa.edu.cn).

Zihao Wang is with the School of Cyber Security, University of Chinese Academy of Sciences, Beijing, 100049, China. (e-mail: wangzihao191@mails.ucas.edu.cn).

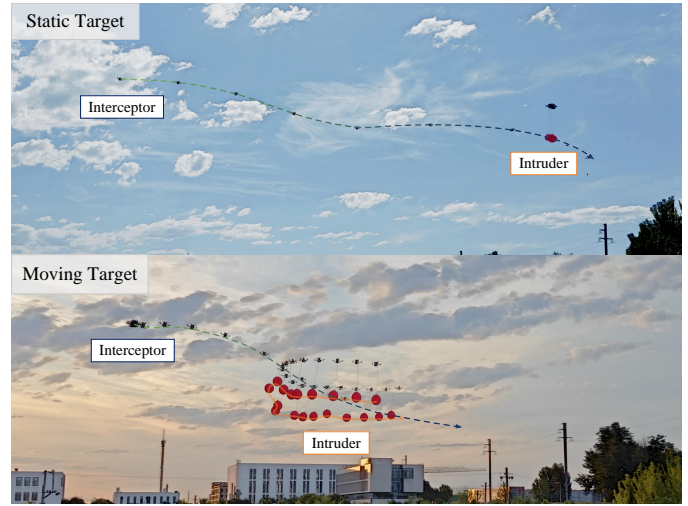


Fig. 1. Intercepting flight target with multicopter.

In recent years, much research has focused on camera-equipped multicopters for intercepting non-cooperative targets. These methods are primarily divided into two categories: Location estimation-based and IBVS-based. Common Location estimation-based methods employ binocular cameras [11], [14], the Kalman filter [13], [15], and geometry-based approaches [16] for target estimation. After that, a trajectory is planned for interception. However, these methods are error-sensitive and limited by sensor perception range and computational performance. Yet the IBVS methods have a simple structure that calculates the control quantity directly from the sensing module. So it offers advantages such as insensitivity to modeling and calibration, fast response, and extended sensing capabilities. These advantages make it a highly competitive solution for interception tasks.

Multicopter IBVS faces significant challenges in precise interception of non-cooperative flight targets. During interception, the observable field of view (FOV) is susceptible to the multicopter's attitude, making it challenging to maintain the 2D visibility required for IBVS [17]. Interception accuracy is further affected by target maneuvers, image processing delay, multicopter dynamics delay, and guidance strategy. In our previous work [18], [19], four and six degree of freedom (DOF) IBVS controllers were designed for low and high speed target interception, respectively. Delayed Kalman filtering (DKF) was proposed in [19] for mitigating image processing delay. Some other studies focus on target observa-

tion innovations. A virtual-plane IBVS scheme [20] decouples multicopter dynamics and uses an improved image error term to reduce the impact of multicopter rotation during 3D target chasing. A pseudo-linear Kalman filter [21] and a 3D helical guidance law enhances observability for intruding multicopter tracking. Classic guidance laws, such as the pursuit guidance (PG) method [22], aim for lower off-target interception but are less efficient for moving targets. These methods can cause multicopter overload saturation or loss of the target due to image processing latency, inappropriate guidance strategies, and target maneuvers. No related work has focused on the bad impact of overload on interception accuracy. An ideal flat trajectory at the end phase of interception reduces direction angle measurement errors from image processing latency and provides a greater dynamics margin to handle target maneuvers.

In this paper, an IBVS controller is designed for precision interception of non-cooperative flight targets, inspired by bird-catching behaviors. Birds rely solely on vision for efficient hunting, similar to IBVS methods for multicopter interception tasks (see Fig. 1). Specifically, the trajectory of a peregrine falcon hunting mallard duck could be described by proportional navigation guidance (PNG) [23], inspired our use of PNG for our tasks. PNG, widely used in missile guidance for decades, flattens the end-phase trajectory and reduces the miss distance [24]. Additionally, a FOV holding controller mimics the bird's neck rotation for prey tracking. So the proposed controller can continuously and stably track the target and precise interception like a peregrine falcon. Overall, the contributions of this paper are summarized as follows:

- 1) The proposed algorithm achieved a Circular Error Probability (CEP) of 0.089 meters in typical tests, improving interception accuracy from the decimeter level of recent algorithms [19] to the centimeter level. CEP is a measure where there is a 50% probability that the interceptor will hit within a circle centered on the target with the given radius [25].
- 2) A FOV holding controller that incorporates PNG and multicopter dynamics is designed to enhance robustness in target tracking.
- 3) Real and simulated experiments, with extensive comparisons across various scenarios, validate the effectiveness and accuracy of the proposed algorithms.

The rest of this paper is organized into five parts. Section II presents the basic modeling and algorithmic framework. Details of the IBVS controller design are provided in Section III. Simulation experiments are discussed in Section IV, while real-world experiments are covered in Section V. Finally, Section VI concludes with a summary of findings and directions for future research.

II. MODELS AND FRAMEWORK

A. Coordinate systems and relative motion models

There are four coordinate systems used, as shown in Figure 2: the Earth-Fixed Coordinate System (EFCS): $o_e - x_e y_e z_e$, the Body Coordinate System (BCS): $o_b - x_b y_b z_b$, Camera

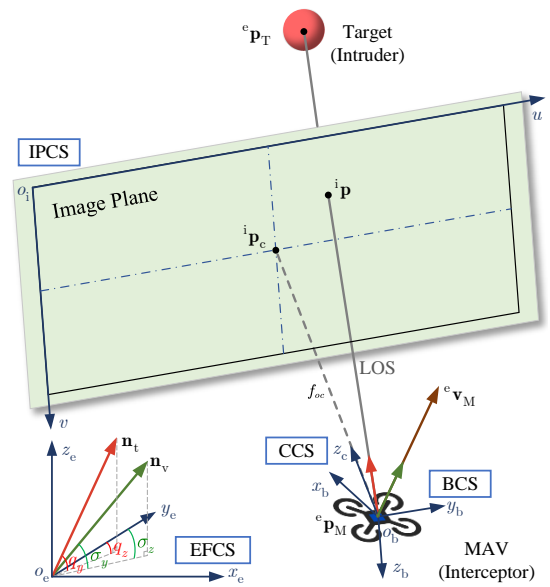


Fig. 2. Coordinate system frames and description of the interception problem. In the earth coordinate system, vector \mathbf{n}_t (red vector) represents the LOS direction, while vector \mathbf{n}_v (green vector) represents the velocity direction. This information is obtained from sensors carried by the drone.

Coordinate System (CCS): $o_c - x_c y_c z_c$ and Image pixel coordinate system (IPCS): $o_i - uv$.

In the relative motion model, both the target (T) and the multicopter (M) are assumed to be point masses. In the EFCS, the relative relationship can be expressed as:

$$\begin{aligned} {}^e \mathbf{p}_r &= {}^e \mathbf{p}_T - {}^e \mathbf{p}_M \\ {}^e \mathbf{v}_r &= {}^e \mathbf{v}_T - {}^e \mathbf{v}_M \\ {}^e \mathbf{a}_r &= {}^e \mathbf{a}_T - {}^e \mathbf{a}_M \\ &= {}^e \mathbf{a}_r^t + {}^e \mathbf{a}_r^n \end{aligned} \quad (1)$$

where ${}^e \mathbf{a}_r^t$ and ${}^e \mathbf{a}_r^n$ represent the relative tangential and normal acceleration in the EFCS, respectively. The relative position ${}^e \mathbf{p}_r$ also denotes the line-of-sight (LOS) between the interceptor and the target.

B. Multicopter Dynamics Model

The multicopter used for interception is modeled as a rigid body with mass m . Its flight control rigid model can be summarized as [26]:

$$\begin{cases} {}^e \dot{\mathbf{p}}_M = {}^e \mathbf{v}_M \\ {}^e \dot{\mathbf{v}}_M = \mathbf{g} + \frac{1}{m} {}^e \mathbf{f} \\ \dot{\mathbf{R}}_b^e = \mathbf{R}_b^e [{}^b \boldsymbol{\omega}]_{\times} \\ \mathbf{J} \cdot {}^b \dot{\boldsymbol{\omega}} = -{}^b \boldsymbol{\omega} \times (\mathbf{J} \cdot {}^b \boldsymbol{\omega}) + \mathbf{G}_a + {}^b \mathbf{M}_d \end{cases} \quad (2)$$

where ${}^e \mathbf{p}_M$ and ${}^e \mathbf{v}_M$ is the multicopter's position and velocity in the EFCS, respectively. \mathbf{g} denotes the acceleration due to gravity, typically represented as $[0 \ 0 \ g]^T$ with $g \approx 9.8 \text{ m/s}^2$. ${}^e \mathbf{f} \in \mathbf{R}^3$ is the controlled lift of the multicopter, directed opposite to the z -axis of the airframe. $\mathbf{R}_b^e \in \text{SO}(3)$ represents the rotation from the BCS to the EFCS; ${}^b \boldsymbol{\omega}$ is

the angular velocity in the BCS, and $[\cdot]_{\times}$ is the cross-product matrix associated with ${}^b\boldsymbol{\omega}$, where $[\cdot]_{\times}$ denotes the matrix such that $[\mathbf{x}]_{\times} \mathbf{y} = \mathbf{x} \times \mathbf{y}$ for any $\mathbf{x}, \mathbf{y} \in \mathbb{R}^3$. \mathbf{J} is the moment of inertia of the multicopter, \mathbf{G}_a represents the gyroscopic moment, and ${}^b\mathbf{M}_d$ denotes the aerodynamic moment associated with propeller steering.

C. Camera Image Model

The multicopter is equipped with a strapdown monocular camera modeled using the pinhole model. This model projects target ${}^c\mathbf{p}_T = [{}^c p_{tx} \ {}^c p_{ty} \ {}^c p_{tz}]^T$ from 3D space to the 2D camera plane: $\mathbb{R}^3 \rightarrow \mathbb{R}^2$. The center point of the target in the IPCS is denoted as ${}^i\mathbf{p} = [u, v]^T$. The error in the IPCS, represented as $\mathbf{e} = [e_x, e_y]^T$, is defined as:

$$\mathbf{e} \triangleq {}^i\mathbf{p} - {}^i\mathbf{p}_c \quad (3)$$

where ${}^i\mathbf{p}_c = [u_0, v_0]^T$ is the geometric centroid of the image in the IPCS. The relationship between the error and the change in camera motion can be described by the Jacobian matrix of the IBVS [27]:

$$\dot{\mathbf{e}} = \mathbf{L}_s {}^c\tilde{\mathbf{v}}, \quad \mathbf{L}_s = \begin{bmatrix} -\frac{1}{{}^c p_{tz}} & 0 & \frac{\bar{e}_x}{{}^c p_{tz}} & \bar{e}_x \bar{e}_y & -(1 + \bar{e}_x^2) & \bar{e}_y \\ 0 & -\frac{1}{{}^c p_{tz}} & \frac{\bar{e}_y}{{}^c p_{tz}} & 1 + \bar{e}_y^2 & -\bar{e}_x \bar{e}_y & -\bar{e}_x \end{bmatrix} \quad (4)$$

where ${}^c\tilde{\mathbf{v}} = [{}^c\mathbf{v}^T \ {}^c\boldsymbol{\omega}^T]^T$ represents the instantaneous linear velocity angular velocity of the camera. $\bar{\mathbf{e}} = [\bar{e}_x \ \bar{e}_y]^T = [e_x/f_{oc} \ e_y/f_{oc}]^T$ represents the normalized image error of features in IPCS, and f_{oc} is the focal length of the camera.

The LOS vector direction $\mathbf{n}_t = [n_{tx} \ n_{ty} \ n_{tz}]^T$, which connects the target and the multicopter in the EFCS, can then be characterized as:

$$\mathbf{n}_t = \frac{{}^e\mathbf{p}_r}{\|{}^e\mathbf{p}_r\|} = \mathbf{R}_b^e \mathbf{R}_c^b \frac{[e_x \ e_y \ f_{oc}]^T}{\|[e_x \ e_y \ f_{oc}]^T\|} \quad (5)$$

where \mathbf{R}_c^b is the rotation matrix from the CCS to the BCS. The LOS vector should not exceed the camera's FOV during interception to fulfill the 2D visibility of the IBVS.

D. Framework overview

The system framework is shown in Fig. 3. First, the image is processed using a target detection algorithm [28], and corrections are estimated using the DKF [19]. The IBVS controller algorithm then calculates the desired lift f_d and angular velocity ω_d for the multicopter flight controller. Finally, the controller generates PWM signals for the motors to execute the target interception.

III. CONTROLLER DESIGN AND ANALYSIS

A. Guidance Algorithm Design

The PNG calculates the rate of change of velocity proportional to the rate of change of the line of sight (LOS), causing

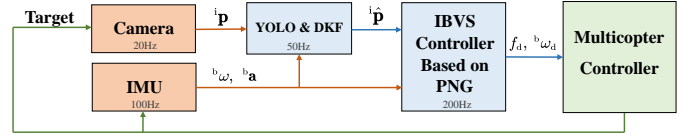


Fig. 3. Framework of proposed IBVS controller based on PNG.

the rate of change of the LOS to become progressively smaller and ultimately achieving interception:

$$\frac{d\sigma}{dt} = K \frac{dq}{dt} \quad (6)$$

where σ is the velocity angle, and q is the LOS angle. K is PNG constant. The trajectory before interception becomes progressively flatter and steadily reaches the target when the value exceeds a certain threshold [24]. However, a value too large can make the controller aggressive and sensitive to noise. The value of K is typically chosen between 2 and 6.

The three-dimensional plane is divided into two two-dimensional planes, as shown in Fig. 2. q_y and q_z are the LOS angles in the vertical and horizontal planes:

$$q_y = \arctan\left(\frac{n_{tz}}{\sqrt{n_{tx}^2 + n_{ty}^2}}\right); q_y \in \left(-\frac{\pi}{2}, \frac{\pi}{2}\right) \quad (7)$$

$$q_z = \arctan\left(\frac{n_{ty}}{n_{tx}}\right); q_z \in (-\pi, \pi).$$

And normalized velocity direction vector $\mathbf{n}_v = [n_{vx} \ n_{vy} \ n_{vz}]^T$. Thus, σ_y and σ_z are the velocity angles in the vertical and horizontal planes which are denoted as:

$$\sigma_y = \arctan\left(\frac{n_{vz}}{\sqrt{n_{vx}^2 + n_{vy}^2}}\right); \sigma_y \in \left(-\frac{\pi}{2}, \frac{\pi}{2}\right) \quad (8)$$

$$\sigma_z = \arctan\left(\frac{n_{vy}}{n_{vx}}\right); \sigma_z \in (-\pi, \pi).$$

Using the integral Eq. (6), desired velocity angle is calculated from the current moment k and the previous moment $k-1$ as:

$$\begin{cases} \sigma_{yd} = K_y (q_y(k) - q_y(k-1)) + \sigma_{y(k-1)} \\ \sigma_{zd} = K_z (q_z(k) - q_z(k-1)) + \sigma_{z(k-1)} \end{cases} \quad (9)$$

where K_y and K_z are proportionality coefficient for the vertical and horizontal planes. Timothy J. Layman *et al.* shows that a value of about 3 is appropriate when multirotor pursuit [29].

Then the desired velocity can be expressed as:

$$\mathbf{v}_d = v_d \mathbf{n}_{vd} \quad (10)$$

where $\mathbf{n}_{vd} = [\sin \sigma_{yd} \cos \sigma_{zd} \ \sin \sigma_{yd} \sin \sigma_{zd} \ \cos \sigma_{zd}]^T$. So the desired velocity can be get by designing the desired velocity magnitude.

B. Field of View Holding Controller

In this subsection, a FOV holding controller is designed to improve the robustness of IBVS during interception. Unlike some control strategies where the z-axis of the CCS is aligned with the target [19] and the target converges to the center of the virtual image plane [20], a new strategy is proposed that aims to:

$$\begin{cases} e_x \rightarrow 0 \\ \Delta e_y \leq \varepsilon \end{cases} \quad (11)$$

Where ε is a small constant and Δe_y is the difference between the largest and smallest e_y during the interception. The primary control objective is to make the target converge to the center in the u-axis direction on the image plane. The secondary control objective is to minimize the range of motion in the v-axis direction.

The causes of target movement in the image plane during interception are analyzed. The main factors are the change of ${}^c\mathbf{p}_r$ due to relative motion and the change in attitude \mathbf{R}_b^e of the multicopter. Due to the role of PNG, the LOS change Δq_g is minimal. Therefore, the focus is on improving target tracking and minimizing the adverse effects of attitude changes by designing a suitable FOV holding controller.

Firstly, the relationship between camera motion and e_x can represent from Eq. (4) as:

$$\dot{e}_x = \begin{bmatrix} -1 & \bar{e}_x \\ c_{p_{tz}} & c_{p_{tz}} \end{bmatrix} c_{\mathbf{v}}^T + [\bar{e}_x \bar{e}_y - (1 + \bar{e}_x^2) \bar{e}_y] c_{\omega}^T. \quad (12)$$

Due to the decoupling of the yaw angle and dynamics of the multicopter, a PD-based controller is designed for improving target tracking:

$${}^b\omega_{\psi} = k_p e_x + k_d \dot{e}_x \quad (13)$$

where k_p and k_d are small negative value. This controller improves the settling time and reduces the overshoot. Furthermore, it helps $e_x \rightarrow 0$ and is insensitive to pixel noise.

Changes in roll angle at greater distances from the target have less impact on the target in the FOV. Therefore, primary attention is given to changes in the pitch angle. To minimize the adverse effects of attitude changes, an acceleration controller is designed as follows:

$$v_d = v_{\text{now}} + k_a \quad (14)$$

where k_a is the velocity gain parameter, typically taken as 1-3. Thus, the dynamics-induced LOS error $\Delta q_d \leq \arctan(k_a/g)$. The change in the LOS angle of the target in the v direction of the IPCS can be expressed as:

$$\Delta q_y = \Delta q_d + \Delta q_g. \quad (15)$$

Based on the geometric relationship, the variation of the target in the image coordinate system can be calculated as:

$$\Delta e_y \leq \frac{v_0 \tan(\Delta q_y)}{\tan(\frac{1}{2}\alpha_{\text{vfov}})} \leq \varepsilon \quad (16)$$

where the parameter α_{vfov} is the angle of the camera's Vertical Field of View (VFOV).

C. Attitude Loop Controller

The desired acceleration is derived from the difference between the desired and current velocities:

$$\mathbf{a}_d = \mathbf{V}_d - \mathbf{V}_{\text{now}} \quad (17)$$

where \mathbf{V}_{now} denotes the current velocity. Based on the multicopter's dynamics model and the equation ${}^e\mathbf{f}_d = f_d \mathbf{n}_{fd}$, the normalized direction of the lift force is:

$$\mathbf{n}_{fd} = \frac{\mathbf{a}_d - \mathbf{g}}{\|\mathbf{a}_d - \mathbf{g}\|}. \quad (18)$$

The attitude \mathbf{R}_d , which incorporates only pitch and yaw, is designed to achieve the desired direction of lift. Here, the rotation matrix that includes only pitch and yaw angles is denoted as $\mathbf{R}_{\text{title}}$. Thus, the desired attitude angle can be expressed as:

$$\begin{aligned} \mathbf{R}_d &= \mathbf{R}_{\text{tilt}} \mathbf{R}_b^e, \\ \mathbf{R}_{\text{tilt}} &= \mathbf{I} + [\mathbf{r}]_{\times} \sin \phi + [\mathbf{r}]_{\times}^2 (1 - \cos \phi) \end{aligned} \quad (19)$$

where $\mathbf{r} = \mathbf{n}_f \times \mathbf{n}_{fd}$, $\phi = \arccos(\mathbf{n}_f^T \mathbf{n}_{fd})$. To achieve the desired pose as described above, a Lyapunov candidate function is formulated as:

$$L = \text{tr}(\mathbf{I} - \mathbf{R}_d \mathbf{R}_b^e). \quad (20)$$

Given that $\|\mathbf{I} - \mathbf{R}_d^T \mathbf{R}_b^e\|_F = \sqrt{2 \text{tr}(\mathbf{I} - \mathbf{R}_d^T \mathbf{R}_b^e)}$, $L = \|\mathbf{I} - \mathbf{R}_d^T \mathbf{R}_b^e\|_F^2 / 2 \geq 0$, the derivative of the candidate function is:

$$\begin{aligned} \dot{L} &= -\text{tr}(\mathbf{R}_d^T \mathbf{R}_b^e [{}^b\omega]_{\times}) \\ &= \text{vex}(\mathbf{R}_d^T \mathbf{R}_b^e - \mathbf{R}_b^{eT} \mathbf{R}_d)^T \mathbf{b}\omega. \end{aligned} \quad (21)$$

To make $\dot{L} \leq 0$ for stability, the pitch and roll angular velocity controllers are designed as:

$${}^b\omega_1 = -\text{vex}(\mathbf{R}_d^T \mathbf{R}_b^e - \mathbf{R}_b^{eT} \mathbf{R}_d). \quad (22)$$

In this context, the attitude control loop for the multi-rotor interceptor can be generalized:

$$\begin{cases} {}^b\omega_d = \text{sat}({}^b\omega_1 + {}^b\omega_2, \omega_m) \\ f_d = \min(\max(\mathbf{n}_f^T (\mathbf{a}_d - m\mathbf{g}), 0), f_m) \end{cases} \quad (23)$$

where ${}^b\omega_1 = [{}^b\omega_{\psi} \ 0 \ 0]^T$. ω_m and f_m denote the maximum angular velocity and maximum lift of the multicopter, respectively. The saturation function of angular velocity $\text{sat}(\cdot)$ is defined as:

$$\text{sat}(\omega, w_m) = \begin{cases} \omega, & \|\omega\| \leq w_m \\ \frac{w_m}{\|\omega\|} \omega, & \|\omega\| > w_m \end{cases}.$$

where it is considered to affect the convergence speed but not the system's stability [19].

IV. SITL EXPERIMENTS

A. Platform introduction and experimental design

In this section, the proposed algorithm is validated and compared using SITL simulation experiments with RflySim [30]. These simulations replicate the architecture and algorithms of real flight experiments, ensuring high fidelity and ease of portability. First, a multi-angle static target interception

experiment is designed to verify the accuracy of the proposed algorithm. Next, moving target interception experiments are performed and compared with other algorithms. These experiments include targets with three common motion models and initial relative positions in three different directions.

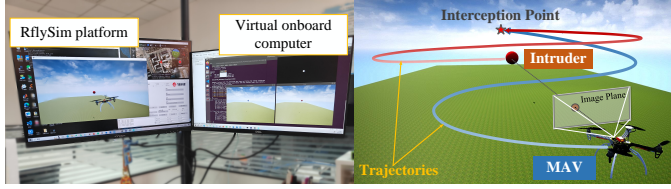


Fig. 4. SITL Platform and Simulation Scenario.

B. Static Target Intercept Simulation Experiments

Fifty static target interception experiments are performed with targets at various locations. The multicopter starts at the position (0,0,10) meters in the EFCS, while the target positions, as shown in Fig. 5(a), are randomly generated between 15 and 35 meters from the multicopter. The multicopter's initial velocity is set to be directly forward, and $k_a = 2$, $K_y = K_z = 3$, $k_p = -0.03$, $k_d = -0.01$ are set.

Experimental results demonstrate that the proposed algorithm accurately intercepts most targets within the FOV. The target distribution in the image plane before interception is shown in Fig. 5(c). The interception error box and CEP are illustrated in Fig. 5(b) and Fig. 5(d), respectively. Compared to previous works [18] and [19], which reported $CEP_{[18]} = 0.457$ m and $CEP_{[19]} = 0.332$ m, the proposed algorithm achieves a $CEP_{\text{Proposed}} = 0.089$ m, representing reductions of 80.5% and 73.2%, respectively. This indicates that the proposed algorithm enhances the accuracy of static target interception from the decimeter level to the centimeter level in the simulation experiments.

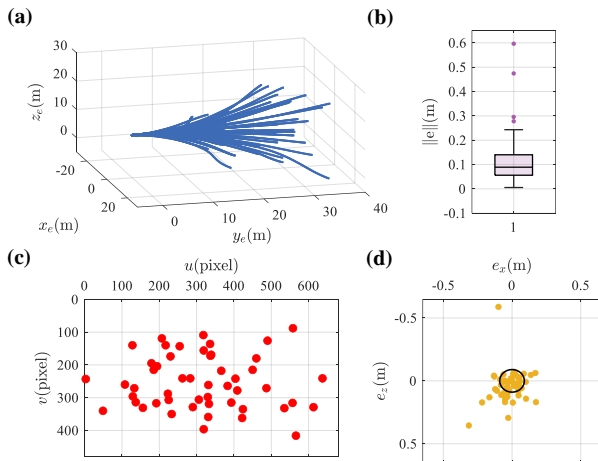


Fig. 5. Experiment results of static target interception simulation: (a) multicopter trajectories, (b) boxplots of interception error, (c) initial target positions in image plane, and (d) interception error distribution.

C. Moving Target Intercept Simulation Experiments

This experiment evaluates the interception accuracy of the proposed algorithm across various target maneuvering scenarios. Three maneuvering models were tested: constant velocity (CV), constant acceleration (CA), and sinusoidal maneuver (SM). Parameters were consistent with those used for intercepting stationary targets. The initial relative positions included three interception scenarios: top-to-bottom, flanking, and tailgate, as shown in Fig. 6. Initially, the interceptor multicopter hovers at (0, 0, 10) m. The target follows three different maneuvering models starting from (0, 25, 1) m, (-8, 15, 8) m, and (0, 30, 10) m, respectively. The models are expressed as:

$$\begin{cases} \text{CV} : {}^e\mathbf{v}_T = (0, 0, 1) \\ \text{CA} : {}^e\mathbf{a}_T = (0.8, 0, 0.2) \\ \text{SM} : {}^e\mathbf{p}_T = (2 \sin(2\pi/14t), 3t, 0) \end{cases}$$

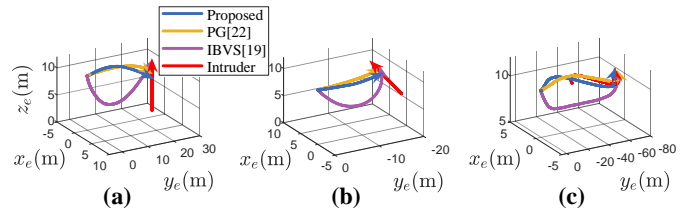


Fig. 6. Trajectory of (a) CV, (b) CA, and (c) SM maneuvering model during moving target interception simulation.

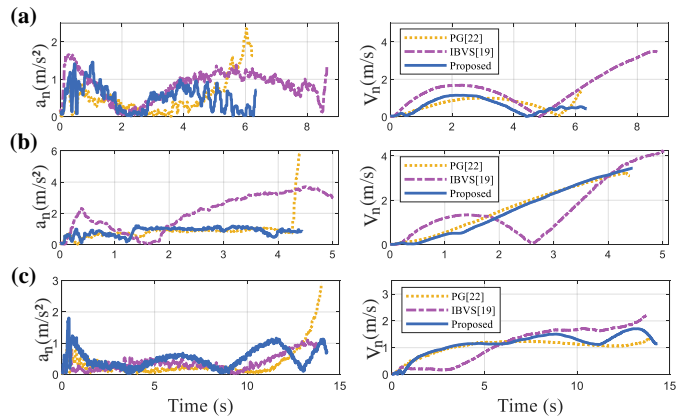


Fig. 7. Normal velocity and normal acceleration of (a) CV, (b) CA, and (c) SM maneuvering model during moving target interception simulation.

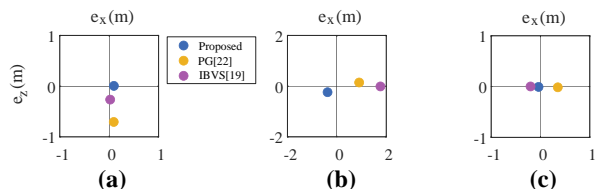


Fig. 8. Errors of (a) CV, (b) CA, and (c) SM maneuvering model in moving target interception simulation.

TABLE I
INTERCEPTION ERROR OF EXPERIMENTS.

Experimental indicators	PG [22]	IBVS [19]	Proposed
Errors of CV model (m)	0.71	0.27	0.09
Errors of CA model (m)	0.92	1.76	0.45
Errors of SM model (m)	0.31	0.20	0.04

Experimental results demonstrate that the proposed algorithm achieves the highest interception accuracy in the simulations. Fig. 7 show the variations in normal acceleration and velocity during interception. The proposed algorithm maintains low normal acceleration and velocity, which is ideal for minimizing interception errors. Low normal acceleration reduces trajectory deviations, while low normal velocity minimizes the impact of image processing delays on accuracy. Interception errors are illustrated in Fig. 8. Table I confirms that the proposed algorithm outperforms the other two algorithms.

Additionally, the effectiveness of the FOV holding controller is evaluated by comparing it with another algorithm. The median, quartiles, boundaries, and outliers of the target in the image plane are shown in Fig. 9. The proposed method exhibits a smaller error variation range than the compared algorithm [19], indicating superior field of view holding capability. This demonstrates the proposed algorithm's greater potential to handle more complex target maneuver scenarios.

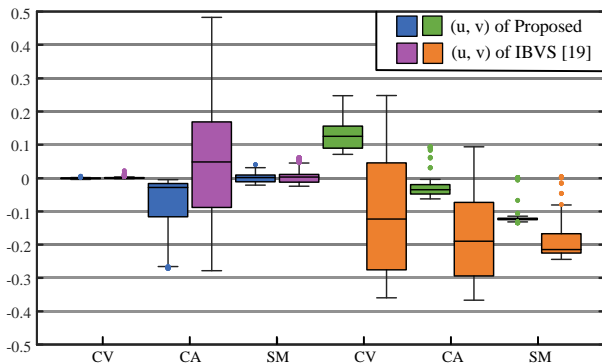


Fig. 9. Normalized image plane error comparison.

V. REAL FLIGHT EXPERIMENTS

A. Introduction to Flight Experiments

Real flight experiments are designed to verify the robustness and effectiveness of the proposed algorithm under more complex conditions. The algorithms, architectures, and parameter settings are the same as in the simulation: $k_a = 2$, $K_y = K_z = 3$, $k_p = -0.03$, $k_p = -0.01$. The real-world experiments are depicted in Fig. 10. The intruder is a red balloon attached to a multicopter by a rope. The interceptor is another multicopter equipped with several components. At the front is a Jetson CSI monocular camera with a 120-degree FOV for capturing images. Behind it is an NVIDIA Jetson Xavier NX, which serves as the onboard computer for processing sensor information and generating control commands. A Pixhawk Nano V5

handles flight control, generating PWM signals to the motors. Additionally, the interceptor is equipped with an RTK module for data analysis target localization (note: this module is not used during the interception process). A video of the flight experiments can be found at <https://youtu.be/sQdRCgnRp4g>.

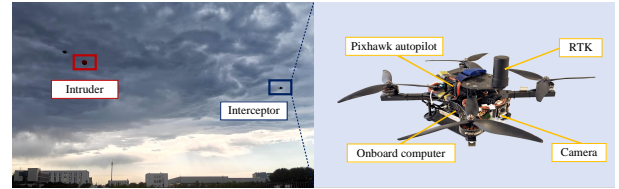


Fig. 10. Real-world flight experiments and hardware architectures for intercepting drones.

B. Static Target Intercept Flight Experiment

The interceptor drone starts from a standstill to intercept a red balloon shaking in the wind about 10m away. The results of the experiment are shown in Figure 11. And the trajectory is shown in (a) and (b). As shown in (c), the target always stays in the FOV during interception and moves only a small range. It proves the effectiveness of the proposed FOV holding controller in the real world. The normal acceleration change little during the whole interception process can be seen in (d). And As shown in (e), normal velocity keep at a small level and the maximum velocity is more than 6m/s.

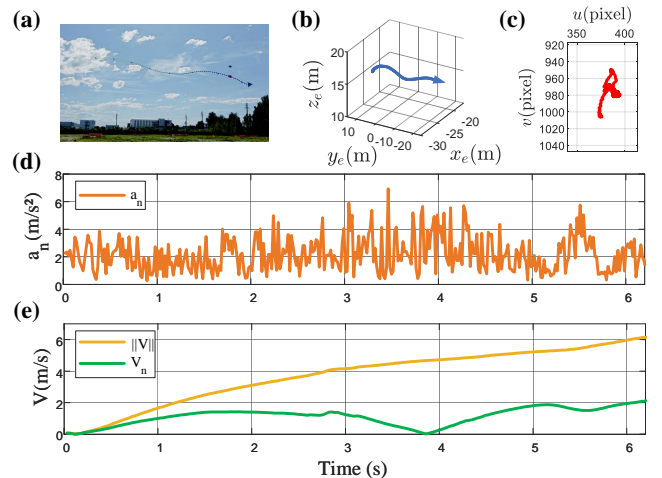


Fig. 11. Results of a flight experiment to intercept a static target.

C. Moving Target Intercept Flight Experiments

Three interception experiments of different maneuver targets are designed: accelerated escape, uniform takeoff, and circular trajectory. These experiments are challenging due to the manoeuvrability of the target and the effects of wind in the field. The relevant initial settings are the same as for the static interception experiment. The interceptor multicopter start the interception task from a standstill. Scenarios and interception trajectory can be seen in Fig. 12. The starting positions are about 10m according to the target.

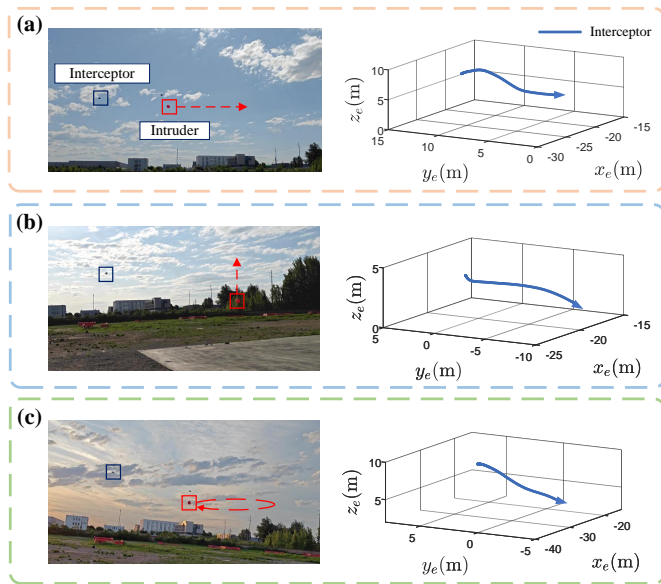


Fig. 12. Schematic of (a) accelerated escape, (b) uniform takeoff, and (c) circular trajectory flight targets and interceptor trajectories.

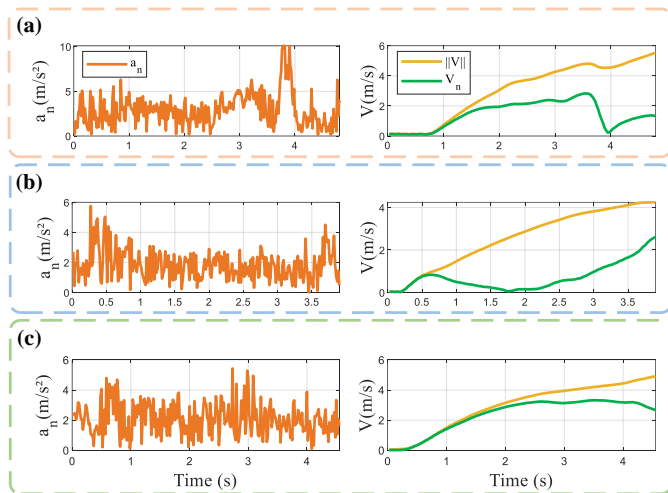


Fig. 13. Normal accelerations, velocities, and normal velocities of the interceptor during the interception of (a) accelerated escape, (b) uniform takeoff, and (c) circular trajectory flight targets.

All three intercept experiments successfully achieved interception of maneuvering targets. The time taken for interception was approximately 4.8s, 3.9s, and 4.6s, respectively. The velocity and normal acceleration during interception can be seen in Fig. 13. At the end stage of interception, the normal acceleration and normal velocity of the interceptor were essentially the same as those in the hovering stage. The final interception speeds were around 5 m/s. During the interception of the accelerated escape target and the circular trajectory target, a significant portion of the interceptor's velocity was used for normal velocity in the early stage. This indicates that the PNG works to ensure a flat trajectory by constantly adjusting the relative position before interception. Recorded trajectories further demonstrate the effectiveness of the proposed guidance law in intercepting maneuvering targets.

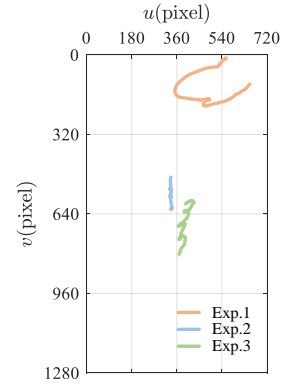


Fig. 14. The trajectory of the target in image plane when intercepting a maneuvering target.

Additionally, all experiments maintained the target within the FOV during interception. The position of the target in the image plane can be seen in Fig. 14. Generally, all targets moved within a small area in the middle of the image. Despite some dispersion in the first experiment when intercepting the accelerated escape target, the results prove the effectiveness and robustness of the proposed FOV holding controller in intercepting maneuvering targets in real scenarios.

D. Compare Intercept Flight Experiments

However, the two most relevant algorithms [19] and [22] were tested for intercepting an accelerated escape target. This maneuver model is considered the most challenging by previous experiments. As shown in Fig. 15, both algorithms failed during the interception and were subsequently returned by manual remote control. After analysis, the reasons for the interception failure of these two algorithms may be: (1) The overload during interception exceeds the dynamics range of the multicopter, causing the target to exceed the FOV. (2) Random wind disturbances during the experiments result in irregular balloon oscillations. (3) Two algorithms' interception accuracy are larger than the size of the balloon.

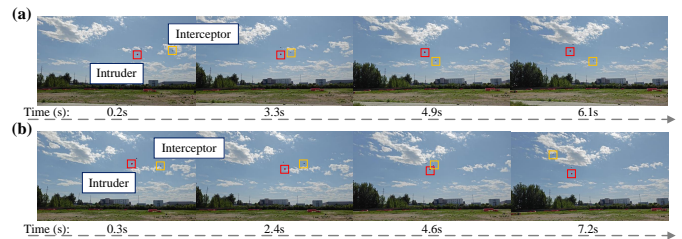


Fig. 15. Snapshots of comparative challenging interception experiments for intercepting accelerated escape targets. Both contrasting algorithms of (a) [19] and (b) [22] failed.

VI. CONCLUSION

In this paper, an IBVS algorithm based on PNG was designed to address the problem of intercepting non-cooperative flight targets with a multicopter. The flat trajectory generated by PNG reduces errors due to image processing latency,

thereby improving interception accuracy. Additionally, the proposed algorithm demonstrates increased robustness through the FOV holding controller designed for the multicopter. Extensive simulation and real flight experiments have validated the accuracy of the proposed algorithm's interception capability. However, the proposed algorithm may face challenges when intercepting higher-speed targets. Therefore, future work will focus on enhancing guidance law applications and employing more precise control methods.

REFERENCES

- [1] H. Wei, B. Lou, Z. Zhang, B. Liang, F.-Y. Wang, and C. Lv, "Autonomous navigation for evtol: Review and future perspectives," *IEEE Transactions on Intelligent Vehicles*, vol. 9, no. 2, pp. 4145–4171, 2024.
- [2] L. Qiao, S. Li, Y. Zhang, and J. Yan, "Early wildfire detection and distance estimation using aerial visible-infrared images," *IEEE Transactions on Industrial Electronics*, pp. 1–11, 2024.
- [3] F. Hong, G. Wu, Q. Luo, H. Liu, X. Fang, and W. Pedrycz, "Logistics in the sky: A two-phase optimization approach for the drone package pickup and delivery system," *IEEE Transactions on Intelligent Transportation Systems*, vol. 24, no. 9, pp. 9175–9190, 2023.
- [4] K. Liu and B. M. Chen, "Industrial uav-based unsupervised domain adaptive crack recognitions: From database towards real-site infrastructural inspections," *IEEE Transactions on Industrial Electronics*, vol. 70, no. 9, pp. 9410–9420, 2023.
- [5] S. Liaquat, M. Faizan, J. N. Chattha, F. A. Butt, N. M. Mahyuddin, and I. H. Naqvi, "A framework for preventing unauthorized drone intrusions through radar detection and gps spoofing," *Ain Shams Engineering Journal*, vol. 15, no. 5, p. 102707, 2024.
- [6] S. Wu, Y. Li, Z. Wang, Z. Tan, and Q. Pan, "A highly interpretable framework for generic low-cost uav attack detection," *IEEE Sensors Journal*, vol. 23, no. 7, pp. 7288–7300, 2023.
- [7] M. Z. Chaari, "Testing the efficiency of laser technology to destroy the rogue drones," *Security and Defence Quarterly*, vol. 32, pp. 31–38, 11 2020.
- [8] Science Focus, "Drone-killer fires microwave beams to disable uavs," <https://www.sciencefocus.com/future-technology/drone-killer-fires-microwave-beams-to-disable-uavs/>, Feb. 2022, accessed on 18 February 2022.
- [9] Y. Chen, Z. Li, L. Li, S. Ma, F. Zhang, and C. Fan, "An anti-drone device based on capture technology," *Biomimetic Intelligence and Robotics*, vol. 2, no. 3, p. 100060, 2022.
- [10] D. Dynamics, "Dronecatcher," www.dronecatcher.nl, 2021.
- [11] M. Vrba, D. Heřt, and M. Saska, "Onboard marker-less detection and localization of non-cooperating drones for their safe interception by an autonomous aerial system," *IEEE Robotics and Automation Letters*, vol. 4, no. 4, pp. 3402–3409, 2019.
- [12] M. Vrba, Y. Stasinchuk, T. Báča, V. Spurný, M. Petrлік, D. Heřt, D. Žaitlík, and M. Saska, "Autonomous capture of agile flying objects using uavs: The mbzirc 2020 challenge," *Robotics and Autonomous Systems*, vol. 149, p. 103970, 2022.
- [13] H. Tao, D. Lin, S. He, T. Song, and R. Jin, "Optimal terminal-velocity-control guidance for intercepting non-cooperative maneuvering quadcopter," *Journal of Field Robotics*, vol. 39, no. 4, pp. 457–472, 2022.
- [14] A. Barišić, F. Petric, and S. Bogdan, "Brain over brawn: Using a stereo camera to detect, track, and intercept a faster uav by reconstructing the intruder's trajectory," *Field robotics*, vol. 2, no. 1, pp. 222–240, 2022.
- [15] A. Agrawal, A. Bhise, R. Arasanipalai, L. A. Tony, S. Jana, and D. Ghose, *Accurate Estimation of 3D-Repetitive-Trajectories using Kalman Filter, Machine Learning and Curve-Fitting Method for High-speed Target Interception*, pp. 93–122. Cham: Springer International Publishing, 2023.
- [16] Y. Stasinchuk, M. Vrba, M. Petrлік, T. Báča, V. Spurný, D. Hert, D. Žaitlík, T. Nascimento, and M. Saska, "A multi-uav system for detection and elimination of multiple targets," in *2021 IEEE International Conference on Robotics and Automation (ICRA)*, pp. 555–561, 2021.
- [17] N. Guenard, T. Hamel, and R. Mahony, "A practical visual servo control for an unmanned aerial vehicle," *IEEE Transactions on Robotics*, vol. 24, no. 2, pp. 331–340, 2008.
- [18] K. Yang and Q. Quan, "An autonomous intercept drone with image-based visual servo," in *2020 IEEE International Conference on Robotics and Automation (ICRA)*, pp. 2230–2236, 2020.
- [19] K. Yang, C. Bai, Z. She, and Q. Quan, "High-speed interception multicopter control by image-based visual servoing," *IEEE Transactions on Control Systems Technology*, pp. 1–17, 2024.
- [20] G. Wang, J. Qin, Q. Liu, Q. Ma, and C. Zhang, "Image-based visual servoing of quadrotors to arbitrary flight targets," *IEEE Robotics and Automation Letters*, vol. 8, no. 4, pp. 2022–2029, 2023.
- [21] J. Li, Z. Ning, S. He, C.-H. Lee, and S. Zhao, "Three-dimensional bearing-only target following via observability-enhanced helical guidance," *IEEE Transactions on Robotics*, vol. 39, no. 2, pp. 1509–1526, 2023.
- [22] S. Jana, L. A. Tony, A. A. Bhise, V. Varun, and D. Ghose, "Interception of an aerial manoeuvring target using monocular vision," *Robotica*, vol. 40, no. 12, pp. 4535–4554, 2022.
- [23] C. H. Brighton, A. L. R. Thomas, and G. K. Taylor, "Terminal attack trajectories of peregrine falcons are described by the proportional navigation guidance law of missiles," *Proceedings of the National Academy of Sciences of the United States of America*, vol. 114, pp. 13 495–13 500, 2017.
- [24] M. Guelman, "A qualitative study of proportional navigation," *IEEE Transactions on Aerospace and Electronic Systems*, no. 4, pp. 637–643, 1971.
- [25] D. Shnidman, "Efficient computation of the circular error probability (cep) integral," *IEEE Transactions on Automatic Control*, vol. 40, no. 8, pp. 1472–1474, 1995.
- [26] A. Abdessameud and F. Janabi-Sharifi, "Image-based tracking control of vtol unmanned aerial vehicles," *Automatica*, vol. 53, pp. 111–119, 2015.
- [27] F. Chaumette and S. Hutchinson, "Visual servo control. i. basic approaches," *IEEE Robotics & Automation Magazine*, vol. 13, no. 4, pp. 82–90, 2006.
- [28] C.-Y. Wang, A. Bochkovskiy, and H.-Y. M. Liao, "Yolov7: Trainable bag-of-freebies sets new state-of-the-art for real-time object detectors," in *2023 IEEE/CVF Conference on Computer Vision and Pattern Recognition (CVPR)*, pp. 7464–7475, 2023.
- [29] T. Layman, T. Fields, and O. A. Yakimenko, "Evaluation of proportional navigation for multirotor pursuit," in *AIAA Scitech 2021 Forum*, p. 1813, 2021.
- [30] X. Dai, C. Ke, Q. Quan, and K.-Y. Cai, "Rflysim: Automatic test platform for uav autopilot systems with fpga-based hardware-in-the-loop simulations," *Aerospace Science and Technology*, vol. 114, p. 106727, 2021.



Hailong Yan received the B.S. degree in mechanical engineering from University of Science and Technology Beijing, Beijing, China, in 2022. He is currently working toward the Ph.D. degree in computer science and technology with the School of Computer Science, Northwestern Polytechnical University, Xi'an, China.

His main research interests include UAV swarm navigation, multicopter visual servo control, and cooperative guidance.



Kun Yang is working toward the Ph.D. degree at the School of Automation Science and Electrical Engineering, Beihang University (formerly Beijing University of Aeronautics and Astronautics), Beijing, China. He received his B.S. degree in North China Electric Power University in 2018, and his M.S. degree in Beihang University in 2021.

His main research interests include vision-based navigation and swarm confrontation.



Yixiao Cheng is currently working toward the B.S. degree in School of Future Aerospace Technology, Beihang University (formerly Beijing University of Aeronautics and Astronautics), Beijing, China.

His main research interests include Synchronization Guidance Algorithm and UAV visual servo control.



Zihao Wang is currently pursuing a Ph.D. in Signal and Information Processing at the School of Cyber Security, University of Chinese Academy of Sciences. He received his B.S. degree in Intelligence Science and Technology from Hunan University in 2019.

His current research interests include UAV swarm navigation, motion planning, and control.



Dawei Li received the B.S. and M.S. degrees in aeronautical and astronautical sciences and technology from Beihang University in 2001 and 2005, respectively, and the Ph.D. degree in control science and engineering from Beihang University in 2013.

He is currently an associate professor with the Institute of Unmanned System at Beihang University. Prof. Li has a strong academic background and practical experience in the field of aircraft design and flight control. His main re-

search interests include micro UAV design, computational fluid dynamics, flight control, and aerial swarm control and navigation.